Hierarchically porous electrospun carbon nanofiber for high-rate capacitive deionization electrodes

John B. Waugh [a,b], Siddharth Komini Babu [a], Qinjun Kang [a], Nicole K. Moehring [b], Angelica Benavidez [c], Xiaojing Wang [a], Piran R. Kidambi [b], Peter N. Pintauro [b], Jacob S. Spendelow [a,*]

[a] Materials Physics and Applications Division, Los Alamos National Laboratory, Los Alamos, NM, USA
[b] Department of Chemical and Biomolecular Engineering, Vanderbilt University, Nashville, TN, USA
[c] Center for Microengineered Materials, Department of Chemical and Biological Engineering, University of New Mexico, Albuquerque, NM, USA

HIGHLIGHTS

- Hierarchically porous carbon fibers were prepared by electrospinning.
- Fibers were tested as electrodes for capacitive deionization.
- Pore scale modeling provided insights into effect of pore size distribution.
- Optimization of mesopore and micropore content provided maximum performance

ARTICLE INFO

ABSTRACT

Capacitive deionization (CDI) is a promising technology that has gained interest for the desalination of brackish water. Hierarchically porous carbons are commonly used as electrodes for CDI due to their high surface areas and controlled pore size distributions that maximize ion adsorption capacity and rate. Electrospinning is an effective way of generating carbon nanofibers with high inter-fiber macroporosity that can be further modified to improve surface area, total pore volume, and pore size distribution. This work describes the use of sacrificial mesopore formers in tandem with a micropore etching technique to induce hierarchical porosity in electrospun fibers. Mesopores are formed via the dissolution of silica nanoparticles that are introduced into the fibers during the electrospinning step. After mesopore formation, micropores are etched into the resulting surface through KOH impregnation and thermal activation. This sequential technique creates a hierarchical network of pores from the inherent macroporosity of the fiber network, to the mesopores, and finally micropores to simultaneously maximize surface area and accessibility. Micropore formation is optimized to maximize specific surface area while maintaining physical integrity of the fibers. The combination of mesopores and micropores enables fast ion adsorption rates and capacity. Carbon fiber electrodes fabricated in this method achieve specific surface areas exceeding 1400 m^2 g^{-1}, with pore volumes exceeding 1.0 cc g^{-1}. The pore size distributions are highly controlled, with 80 % of total pore volume coming from pores <20 nm in radius. In 500 ppm constant voltage CDI tests, these fiber electrodes obtain a salt adsorption capacity of over 14 mg g^{-1} at a salt adsorption rate of ~4 mg g^{-1} min^{-1}, showcasing the high capacity matched with high rate of these easily fabricated, inexpensive materials.

1. Introduction

Freshwater scarcity is a global problem that affects billions of people every year and is worsening as industrial and agricultural growth exacerbate already limited supplies of fresh water [1]. Increasing demand necessitates the development of new technologies to produce fresh water in cost-effective and environmentally friendly ways. Desalination is one such technology, with current processes including reverse osmosis

---

* Corresponding author.
  E-mail address: spendelow@lanl.gov (J.S. Spendelow).

(RO), electrodialysis, and multi-stage flash distillation (MSF). The majority of current water desalination involves RO of seawater (>35,000 ppm TDS), accounting for nearly 70 % of operating seawater desalination plants [2,3]. One facet of desalination technology attracting more attention is brackish water (<20,000 ppm TDS) desalination, which is relatively less expensive due to the lower energy consumption required for desalination at lower salt concentration. Over the last 30 years, brackish water desalination has increased to account for 20 % of global desalination capacity [3].

Capacitive deionization (CDI) has attracted increasing attention as a viable technology for brackish water desalination [4,5]. CDI offers advantages of low voltage operation, low energy consumption, and high energy recovery. High surface area carbon materials are used as capacitive electrodes to provide ample sites for ion adsorption [6–9]. When voltage is applied, ions are adsorbed onto the electrode, yielding a freshwater output stream. When the applied potential is removed, the ions desorb from the electrodes to create a concentrated brine stream. Many different electrode materials have been used as CDI electrodes, such as activated carbons, graphene, carbon nanotubes, carbon aerogels, and carbon nanofibers [10–16]. Electrodes must be designed with high surface area, good conductivity, and fast ion diffusion to achieve high salt adsorption capacities and rates. Carbon nanofibers are an attractive option for CDI electrodes because their interconnected network of conductive fibers offers innate macroporosity, surface area, and conductivity [17].

Electrospinning is an effective way of producing carbon nanofibers (CNFs) suitable as CDI electrodes. The most common polymer used as a CNF precursor is polyacrylonitrile (PAN) because it has a high carbon yield while maintaining the fibrous structure post-carbonization [18]. The electrospinning process allows for high tunability of the morphology of CNFs using additives. A common class of additives for electrospun fibers are sacrificial pore formers that are removed after electrospinning or carbonization to introduce intra-fiber mesoporosity, thus increasing surface area and facilitating ion diffusion. Such pore formers include decomposable organics such as PMMA, PVP, β-cyclodextrin, and $DMSO_2$ [19–22] in addition to inorganic compounds such as $Ni(NO_3)$, $ZnCl_2$, $Zn(Ac)_2$, and SiO_2 [23–27]. These additives are optimized to maximize surface area and diffusion characteristics without compromising the physical properties of the resultant fibers, namely conductivity and mechanical strength. Inducing mesoporosity is helpful for increasing ion transport but is not as effective at increasing surface area. To maximize surface area and capacitance, microporosity must be created through treatments such as KOH etching [28–31]. However, hierarchical porosity must be employed to increase surface area and capacitance (through microporosity) while maintaining fast ion diffusion and salt adsorption rates (through mesoporosity) [32].

In this work, hierarchically porous CNFs were produced using SiO_2 as a mesopore former and KOH as a micropore etching agent to improve pore volume and surface area, as shown in Fig. 1. The SiO_2 was added to the PAN precursor ink to be continuously distributed throughout the fibers during electrospinning. After carbonization, the SiO_2 was dissolved out of the fibers without compromising the fiber's structure, yielding a highly monodisperse pore size distribution. Next, micropores were formed on the already porous fibers, yielding fibers with hierarchical porosity. The resulting CNFs provide excellent CDI performance due to their high porosity, high surface area, and good electrical conductivity. This strategy is unique in its combined utilization of SiO_2/KOH pore formation agents to create a new hierarchically porous fiber electrode that features facile fabrication and tunable porosity. Additional insight into the role of KOH treatment conditions on electrode performance and pore scale modeling of various pore size distributions allow for these findings to be applied to other electrode systems.

2. Experimental

2.1. PAN/SiO₂ ink preparation

In a typical experiment to make 20 % SiO_2 fibers, 0.148 g of SiO_2 (10–20 nm, Sigma Aldrich) was added to 6 g of DMF (>99.8 %, ACS reagent, Sigma Aldrich) and probe sonicated for 24 h (1 s pulse, 4 s off) to disperse and break up the silica agglomerates. Different silica content fibers were made by varying the added silica content relative to the PAN content. Then 0.593 g of Polyacrylonitrile (PAN, 150k MW, Sigma Aldrich) was added to make a 9 wt% solution, relative to DMF content, and stirred at 80 °C overnight. Fibers without SiO_2 added were made with a 10 wt% PAN in DMF solution, stirred at 80 °C overnight.

2.2. Electrospinning of PAN/SiO₂ fibers

PAN/SiO_2 inks were electrospun using a Fluidnatek LE-50 electrospinning system onto a rotating drum equipped with aluminum foil. The electrospinning parameters were as follows: −2 kV collector bias, ~13
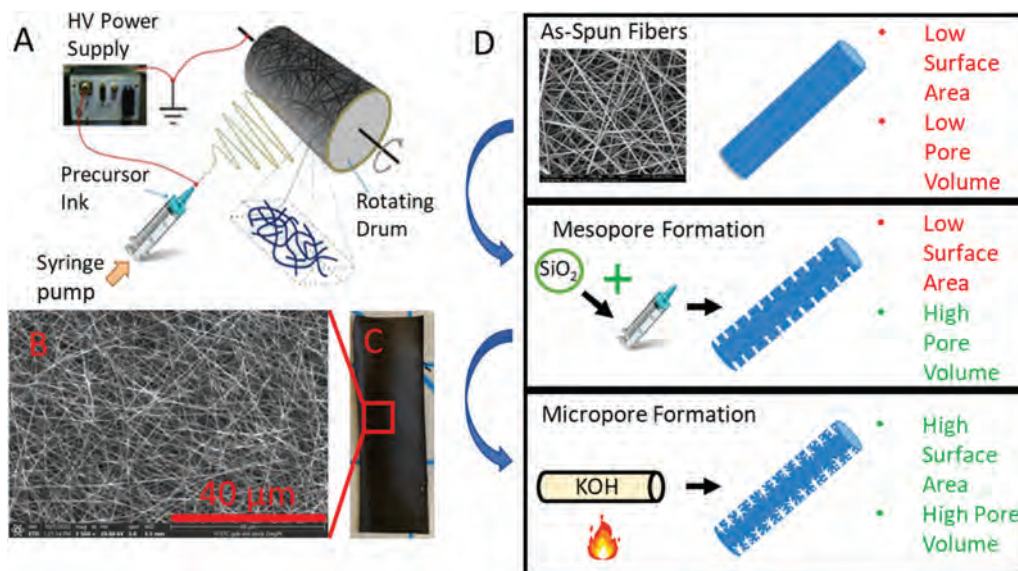

Fig. 1. Design of hierarchically porous CNFs for CDI application. A) Typical electrospinning apparatus. B) Scanning electron micrograph of an electrospun fiber mat. C) Photograph of a free-standing CNF electrode. D) Successive hierarchical pore formation experimental design.

kV applied voltage to needle, 1.0 mL hr^{-1} flow rate, 16 cm tip to collector distance, 200 rpm drum rotation, 22-gauge needle. The resulting polymer fiber mat was cut and stacked to increase mass loading and thickness before heat treatment at 280 °C, 1 °C min^{-1}, for 2 h in ambient air in a muffle furnace. Activated PAN fibers were then carbonized in a tube furnace under N$_2$ flow at 800 °C, with 5 °C min^{-1} ramp rate, for 2 h. The carbonized PAN/SiO$_2$ fibers were then soaked in 3 M NaOH at room temperature overnight to dissolve SiO$_2$, and then soaked in water overnight to remove NaOH. SiO$_2$ removal was evaluated by XRF measurement.

2.3. KOH treatment of PAN/SiO$_2$ fibers

The carbonized fibers were treated using KOH (90 %, reagent grade flakes, Sigma Aldrich) in the following procedure. Carbonized fibers were loaded with 0.8 M KOH solution, drop-wise, until 3× mass was achieved (1,2 fibers, KOH). KOH loaded fibers were then thermally treated in a tube furnace under N$_2$ at varying temperatures (700, 750, 800, 850 °C) with 5 °C min^{-1} ramp rate for 2 h. After treatment, the fibers were washed in water, 1 M HCl, and then water again to remove any remaining KOH or treatment byproducts. All fibers were dried (>80 °C) before being tested. KOH treated fibers were named according to the silica content in the PAN precursor and the KOH treatment temperature (e.g., 20 % SiO$_2$, 800 °C).

2.4. Characterization

The morphology of the fibers was analyzed using field emission scanning electron microscopy (Thermo Scientific Quattro S) and transmission electron microscopy (ThermoFisher Titan 80–300, 300 kV). Specific surface area and pore volumes were measured using N$_2$ adsorption/desorption isotherms at 77 K using a Quantachrome Autosorb iQ$_2$. X-ray photoelectron spectroscopy (XPS) measurements were performed on a Kratos Ultra DLD spectrometer using a monochromatic Al Kα source operating at 150 W and a pressure of 2×10^{-9} Torr. High resolution spectra were acquired at a pass energy of 20 eV and data was processed using Casa XPS software. Raman measurements were performed using a Thermo Scientific DXR Raman Microscope (532 nm, mW laser). Thermogravimetric analysis (TGA) was performed using a TA Instruments TGA Q50 using a 2 °C min^{-1} ramp to 120 °C with a 10 min hold to remove water, then a 10 °C min^{-1} ramp to 800 °C.

2.5. Electrochemical testing

Fiber electrodes were tested in a homemade electrochemical cell using a gold foil current collector in a 3-electrode configuration against a graphite rod counter electrode and an Ag/AgCl reference electrode. Measurements were taken using an SP-200 BioLogic potentiostat. The electrolyte was 1 M NaCl in all electrochemical measurements. Cyclic voltammetry (CV) was performed between 0.5 V and −0.5 V. Electrochemical impedance spectroscopy (EIS) was performed at OCV with 10 mV amplitude between 1 MHz and 5 mHz. Galvanostatic charge discharge (GCD) was performed at varying current densities relative to the dried mass of electrodes between −0.4 V and 0.6 V. Capacitance was evaluated using the following equation:

$$\frac{I_a t_d}{V m_e} \tag{1}$$

where I_a is the applied current, t_d is the discharge time, V is the voltage window of discharge, and m_e is the mass of the electrode.

2.6. Capacitive deionization testing

Fiber electrode CDI performance was evaluated in a flow-through configuration using a compression cell hardware with titanium flow fields, PTFE gaskets to achieve desired compression, and a paper filter separator. All CDI experiments were performed in 500 ppm NaCl at a flow rate of 15 mL min^{-1}. Solution conductivity was measured with a Horiba Laqua 3561 conductivity cell (0.1 cm^{-1} cell constant). Fiber electrodes were cut to 5 cm^2 before cell assembly, and solution was flowed for at least 24 h to achieve equilibrium before applying voltage. The 0 % SiO$_2$ CNFs with no KOH treatment were tested at 0.9 V constant voltage for 5 min to adsorb ions, and then 0 V for 30 min to desorb ions. KOH treated fibers were tested at 1.2 V constant voltage for 5 min followed by 0 V for 30 min. The desorption step was held longer than the adsorption step to cause full removal of salt, as it was observed that shorter desorption steps resulted in diminished SAC. Different voltages were used to test SiO$_2$ CNFs with and without KOH treatment due to higher SAC degradation in the non-KOH treated CNFs. This necessitated use of lower voltages to maintain stable salt adsorption capacities during repeated cycling. Electrodes prepared using the same technique (SiO$_2$ as a mesopore former, KOH micropore formation, or both) were tested at the same applied potential for comparison. The SiO$_2$ CNFs with no KOH treatment were tested at a different voltage because they degraded faster than the KOH treated CNFs, so lower voltages were necessary to maintain stable salt adsorption capacities. CDI experiments were performed in a single-pass method and SAC values (mg g^{-1}) were obtained by integrating the ion adsorption peak, converting to ppm from μS cm^{-1}, multiplying by flow rate (mL s^{-1}), and dividing by combined electrode mass. SAR values were obtained by dividing SAC values by the desorption time.

2.7. Pore scale modeling

Coupled ion transport and adsorption in a cross-section of a single porous fiber was simulated at the pore scale. The diffusion of the ions is governed by the following equation:

$$\frac{\partial C}{\partial t} = \nabla \cdot (D \nabla C), \tag{2}$$

where C and D are ion concentration and diffusion coefficient, respectively. At the pore-carbon interface, the following linear kinetics is considered for ion adsorption:

$$D \frac{\partial C}{\partial n} = k_r C, \tag{3}$$

where n denotes the unit normal perpendicular to the solid surface pointing toward the pore.

The lattice Boltzmann method (LBM) was used to solve Eq. (2), in which the ion diffusion is described by the following equation:

$$g_i(\boldsymbol{x} + \boldsymbol{e}_i \delta t, t + \delta t) - g_i(\boldsymbol{x}, t) = -\frac{1}{\tau} \left(g_i(\boldsymbol{x}, t) - g_i^{eq}(\boldsymbol{x}, t) \right), \tag{4}$$

where g_i is the distribution function along the i direction, g_i^{eq} is the corresponding equilibrium distribution function, δt is the time increment, $\boldsymbol{e}_i$ is the discrete lattice velocity, and τ is the collision time related to the diffusion coefficient. With an appropriate choice of $\boldsymbol{e}_i$ and g_i^{eq}, Eq. (4) can recover Eq. (2), with ion concentration and diffusion coefficient given by $C = \sum g_i$ and $D = \frac{1}{2}(1 - J_0)(\tau - 0.5)$, respectively, where J_0 is a constant between 0 and 1 [33].

3. Results and discussion

3.1. Morphology of porous electrospun fibers

Fig. 2 shows SEM images of CNFs produced using electrospun PAN fiber precursors. Electrospun CNFs produced without pore former showed uniform fiber formation, with an average fiber diameter of 400 nm (±150 nm) and defect-free surfaces (Fig. 2A). 20 % SiO$_2$ CNFs prior to SiO$_2$ dissolution, shown in Fig. 2B, showed SiO$_2$ spread throughout
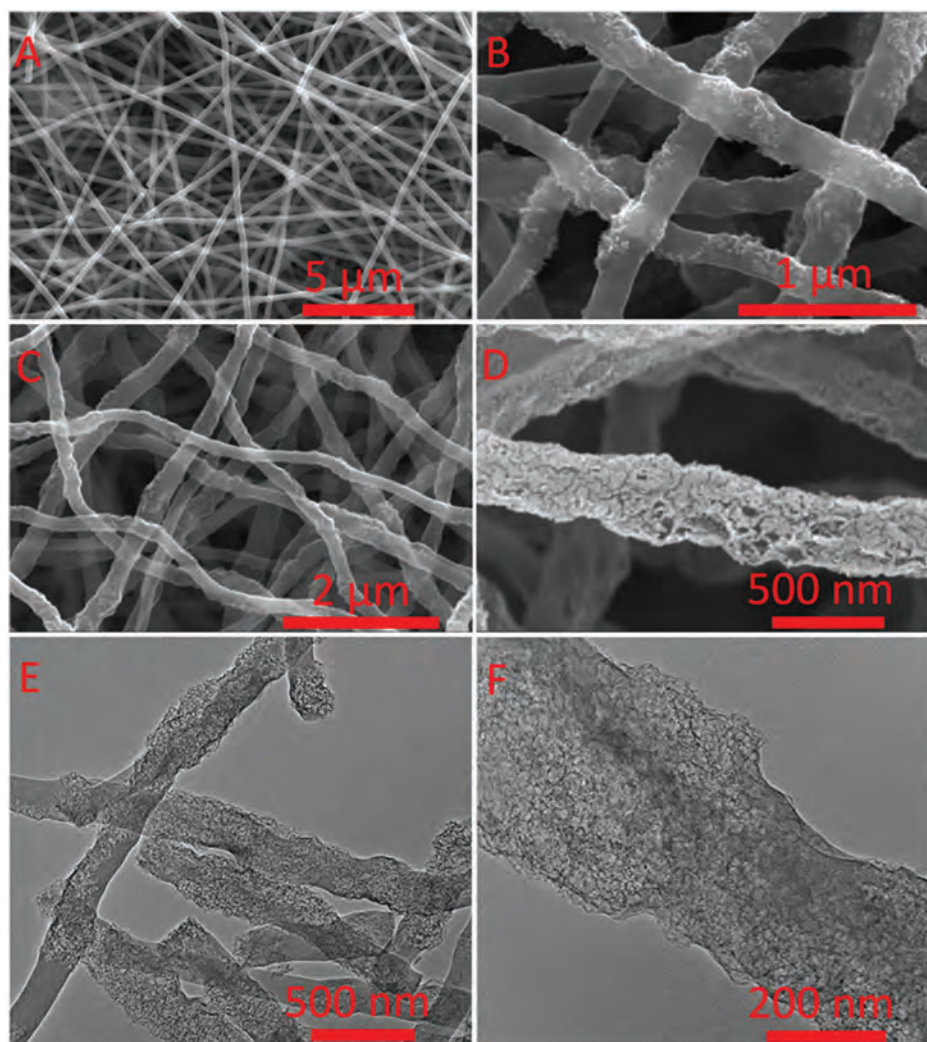
Fig. 2. Scanning electron and transmission electron micrographs of CNFs. A) 0 % SiO$_2$ CNFs. B) 20 % SiO$_2$ CNFs before SiO$_2$ dissolution. C) 20 % SiO$_2$ CNFs after SiO$_2$ dissolution. D) 40 % SiO$_2$ CNFs after SiO$_2$ dissolution and KOH etching. E) TEM images of 20 % SiO$_2$ CNFs after SiO$_2$ dissolution. F) TEM images of 40 % SiO$_2$ CNFs after SiO$_2$ dissolution.

the fibers in small chunks and aggregates. Porous CNFs produced by dissolution of SiO$_2$ from 20 % and 40 % SiO$_2$ PAN CNFs are shown in Fig. 2C and D, respectively. Dissolution of SiO$_2$ yielded mesoporous CNFs with irregular morphology. Larger pores were formed on the surfaces of the fibers in the 40 % SiO$_2$ case, due to aggregation of SiO$_2$ at higher concentrations in the ink. Despite aggregation, each fiber maintained its fibrous structure and showed even distributions of SiO$_2$ throughout, leading to a consistent pore size distribution. The internal porosity of the fibers is visible in TEM images of 20 % SiO$_2$ and 40 % SiO$_2$ CNFs, shown in Fig. 2E and F, respectively. These images show that electrospinning SiO$_2$ into the PAN was effective at distributing the pore former, allowing for mesopore formation throughout the fiber bulk. Removal of SiO$_2$ was evaluated using XRF, which confirmed 97–99 % SiO$_2$ loss after soaking in 3 M NaOH at room temperature, as shown in Table S2, indicating that the dissolution procedure was effective at removing nearly all of the SiO$_2$. Electrospun fibers were etched with KOH after dissolving the SiO$_2$ pore former to create a hierarchically porous structure, shown in Fig. 2D. The SiO$_2$ content of the 0, 20, and 40 wt% PAN fibers was confirmed using TGA, shown in Fig. S1. Non-water mass loss began at 270 °C, in agreement with previous reports of PAN TGA, with plateaus at high temperature indicating leftover SiO$_2$ content [34]. Mass loss was completed by 700 °C, at which point the remaining mass represented the SiO$_2$ content in the CNFs. Excluding water mass,

the 20 % SiO$_2$ fibers were reduced to 19 % remaining mass and the 40 % SiO$_2$ fibers were reduced to 35 % remaining mass. The noticeable discrepancy between the expected and observed mass in the case of the 40 % SiO$_2$ fibers was attributed to the tendency of SiO$_2$ to settle in the high wt% solutions and cling to the sides of the vial, reducing the amount of SiO$_2$ introduced during electrospinning.

The role of SiO$_2$ content in controlling fiber morphology was determined through measurement of the pore size distribution and the specific surface area using nitrogen adsorption-desorption isotherms, as shown in Fig. 3. The adsorption-desorption isotherms for the 0 % SiO$_2$ CNFs showed low gas adsorption, indicating a low surface area and lack of porosity (Fig. 3B). In contrast, CNFs produced using 10–40 % SiO$_2$ pore former exhibited a typical Type IV(a) isotherm shape with a Type H1 hysteresis loop due to the high mesoporosity present in the fibers after pore formation [35–37]. These CNFs showed a pore size distribution with a peak at around 10 nm (Fig. 3A), which resulted from the use of 10–20 nm diameter SiO$_2$ particles as pore formers. Increasing SiO$_2$ content past 20 % caused increased polydispersity, particularly in the case of 40 % SiO$_2$ content. The high SiO$_2$ content in the 40 % SiO$_2$ electrospinning precursor inks caused SiO$_2$ aggregation, resulting in increased presence of larger pores (Fig. 3A). The cumulative pore volume distribution (Fig. 3C) revealed that lower SiO$_2$ contents were effective at creating more defined pore size distributions, as sub-20 nm
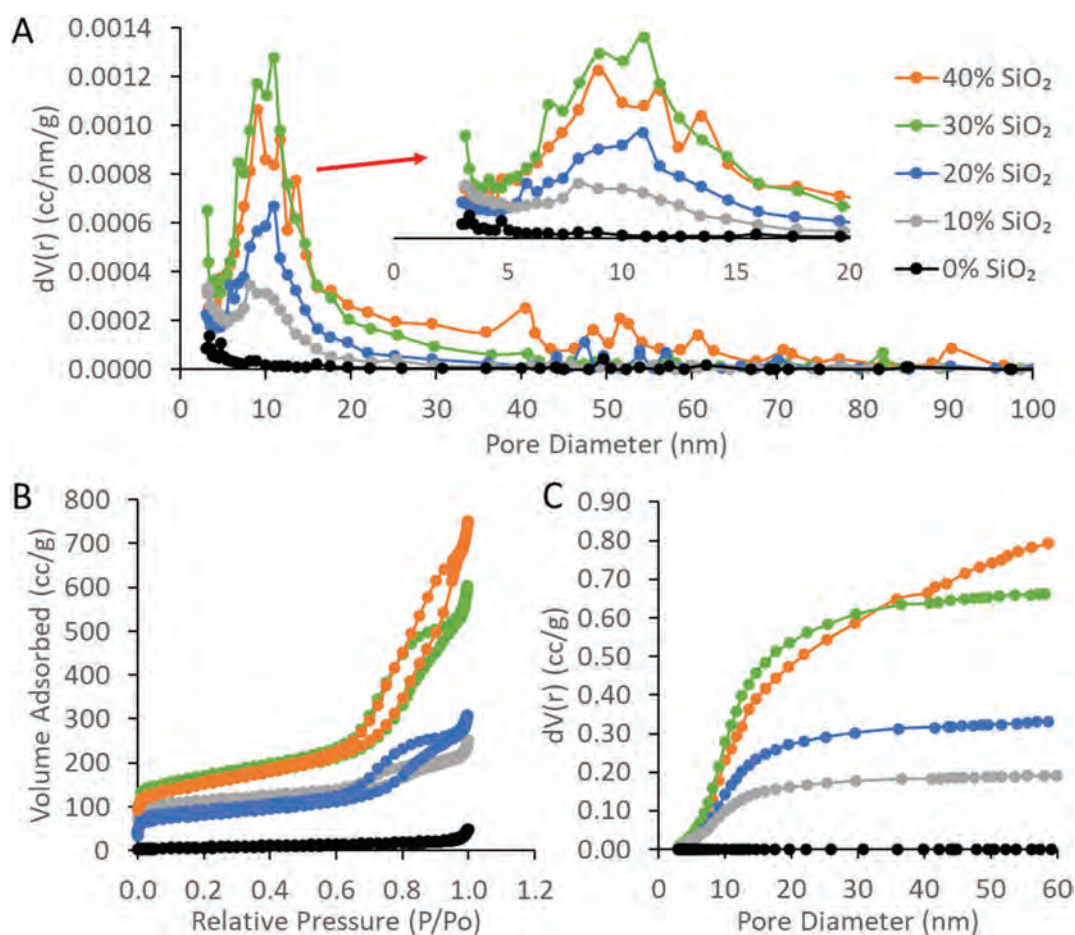
Fig. 3. Nitrogen adsorption/desorption isotherms and modeled pore size distributions for porous CNFs after SiO_2 dissolution. A) BJH pore size distribution, inset of 3–20 nm pore sizes. B) Nitrogen adsorption-desorption isotherms. C) Cumulative pore volume vs. pore size.

pores contributed 80 % of the total porosity in the 20 % SiO_2 CNFs but only ~50 % in the 40 % SiO_2 CNFs. As SiO_2 content was increased, the total pore volume increased from 0.11 cc g^{-1} in 0 % SiO_2 CNFs to a maximum of 1.04 cc g^{-1} in 40 % SiO_2 CNFs, as shown in Table 1. Specific surface area also tended to increase with increasing SiO_2 pore former content, from a minimum SSA of 180 m^2 g^{-1} in 0 % SiO_2 CNFs to a maximum of 476 m^2 g^{-1} in 40 % SiO_2 CNFs. The SSA did not match closely with the pore volume because increasing SiO_2 content tended to induce formation of large pores, inflating the pore volume without greatly increasing SSA due to the lower surface area to volume ratio associated with larger pores.

3.2. Electrochemical and CDI performance of mesoporous fibers

Electrochemical measurements were performed to evaluate the resistance, capacitance, and rate performance of the mesoporous CNFs in 1 M NaCl. Results of these measurements are compared alongside CDI constant voltage desalination results for each SiO_2 content performed in

Table 1
Specific surface area and total pore volume of CNFs produced from PAN with varying content of SiO_2 pore former.

SiO_2 content	SSA (m^2 g^{-1})	Pore volume (cc g^{-1})
40 % SiO_2	476	1.04
30 % SiO_2	474	0.79
20 % SiO_2	252	0.4
10 % SiO_2	305	0.26
0 % SiO_2	180	0.11

500 ppm NaCl at 0.9 V in Fig. 4. All the CNFs prepared using SiO_2 pore former showed more capacitive behavior in EIS experiments compared to 0 % SiO_2 CNFs, as shown in Fig. 4A, indicated by a steeper slope at low frequencies [38,39]. The high-frequency resistances of the fibers were similar, showing that the mesopore formation did not influence the equivalent series resistance significantly. The capacitance measured by GCD was higher in the mesoporous CNFs produced using SiO_2 pore former compared to the 0 % SiO_2 sample, as shown in Fig. 4B. The CNFs based on 40 % SiO_2 pore former achieved the highest capacitance (93 F g^{-1}) at a 0.2 A g^{-1} charging rate, while the 0 % SiO_2 CNFs only reached 45 F g^{-1}. The CNFs based on 10 %, 20 %, and 30 % SiO_2 pore former reached capacitances of 54, 56, and 72 F g^{-1}, respectively. The 20 % SiO_2 fibers exhibited the lowest IR drop of 60 mV at 0.2 A g^{-1}, as shown in Table S3. The 0 % SiO_2 fibers had more than double the iR drop, with 140 mV at 0.2 A g^{-1}. These results indicate that mesopores formed from SiO_2 pore former provided improved benefits to capacitance and resistance up to 20 wt% SiO_2 content.

As current density was increased from 0.2 A g^{-1} to 1.0 A g^{-1}, the iR drop increased significantly. The 0 % SiO_2 CNF sample had a 770 mV drop at 1.0 A g^{-1}, which represents almost the entire charging window. The CNF based on 20 % SiO_2 pore former had the lowest IR drop (280 mV) at 1.0 A g^{-1}, while the CNFs based on 10 %, 30 % and 40 % SiO_2 pore former ranged from 340 to 580 mV. The measured CNF capacitance decreased as current was increased from 0.2 A g^{-1} to 1.0 A g^{-1}, as shown in Fig. 4C. The capacitance of all CNF samples decreased at higher current densities due to the higher iR drop. This limited the potential window of charging, thus lowering capacitance [40]. The lack of porosity in the 0 % SiO_2 CNFs caused a complete loss of capacitance at
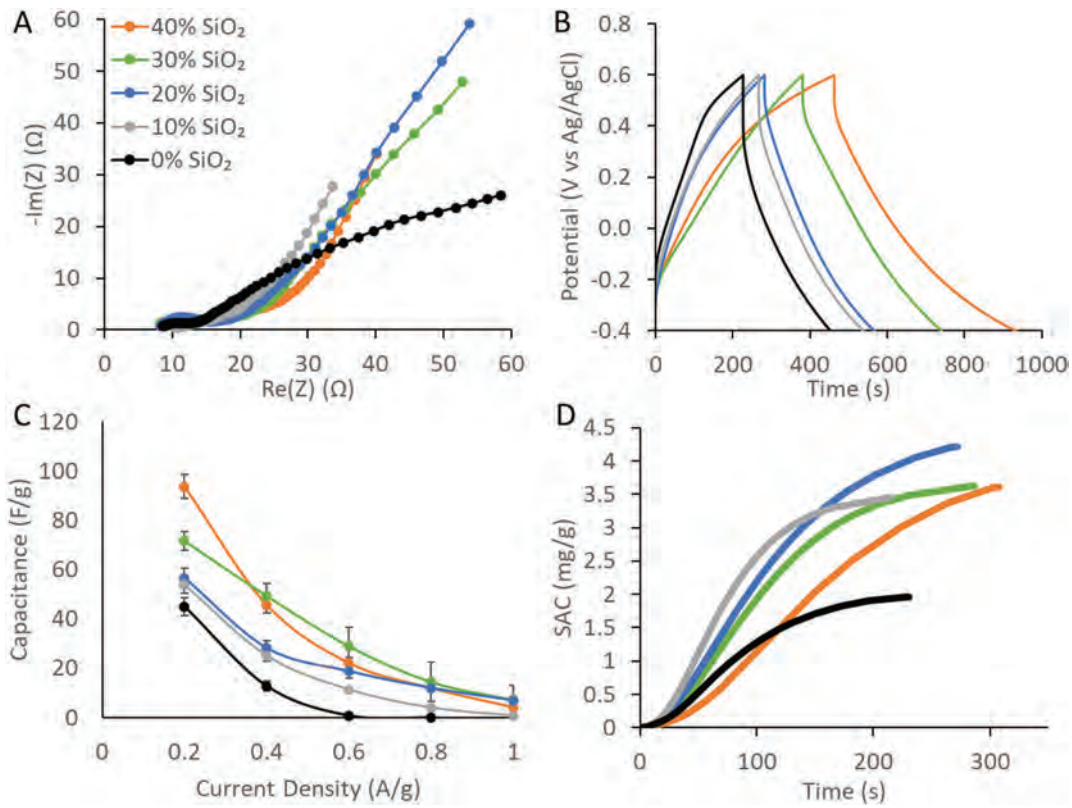
Fig. 4. Electrochemical measurements (performed in 1 M NaCl) and CDI measurements (performed at 0.9 V in 500 ppm NaCl, 15 mL min^{-1} flow rate) of mesoporous CNFs produced using SiO$_2$ pore former. A) EIS spectra. B) Galvanostatic charge/discharge at 0.2 A g^{-1}. C) Capacitance versus current density obtained by GCD. D) SAC vs time obtained by constant voltage desalination.
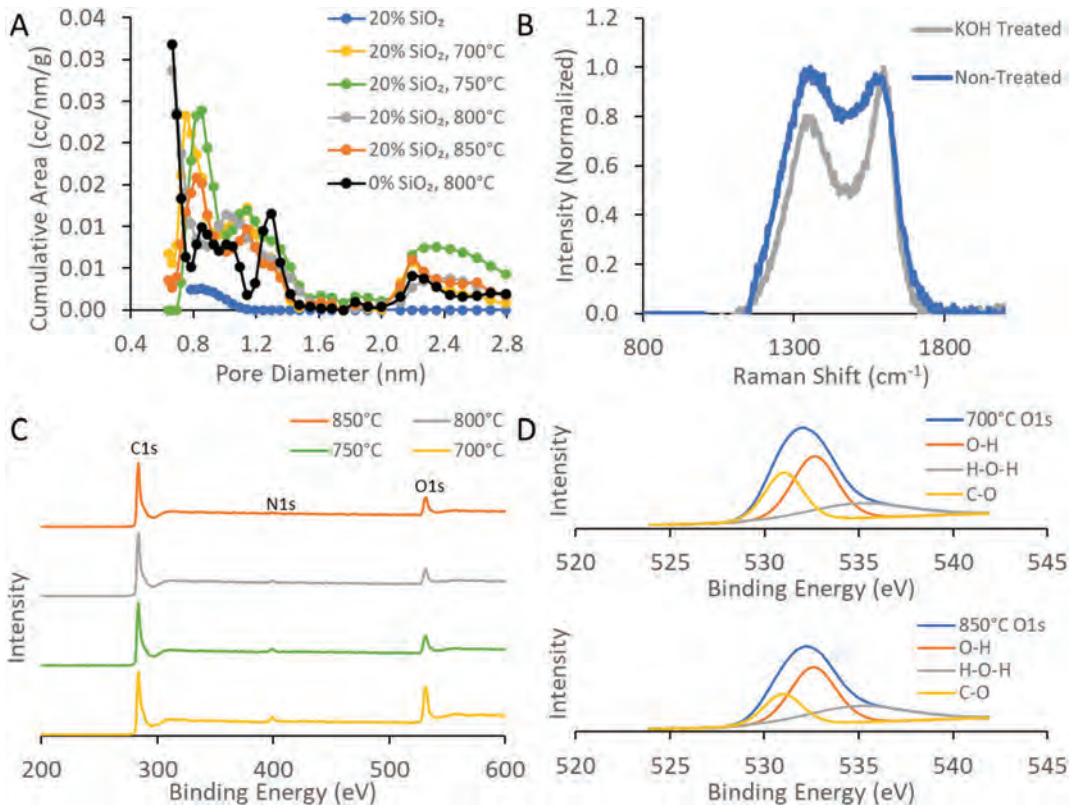

Fig. 5. Characterization of KOH treated CNFs. A) DFT pore size distribution. B) Raman spectra. C) XPS spectra. D) XPS O1s peak spectra.

only 0.6 A g^{-1}, showing how the addition of mesoporosity enhances rate capability significantly [41].

The lower iR drop of the 20 % SiO$_2$ fibers resulted in superior CDI performance, with a SAC of 4.2 mg g^{-1}; the next closest was the 30 % SiO$_2$ CNFs at 3.6 mg g^{-1} SAC, as shown in Fig. 4D. The performance of the 20 % SiO$_2$ CNFs, despite their lower capacitance and SSA compared to the CNFs based on higher SiO$_2$ content, can be attributed to its narrower pore size distribution and lower iR drop. The 20 % SiO$_2$ fibers showed faster salt adsorption than the 30 % and 40 % SiO$_2$ fibers throughout the experiment. The 10 % SiO$_2$ content fibers showed even faster initial salt adsorption rates because of their lower porosity and shorter diffusion pathways, but salt adsorption tapered off as the electrode became saturated more quickly. The charge efficiency of these electrodes is shown in Table S2, where the 20 % SiO$_2$ CNFs obtained the highest charge efficiency of 0.44 at 0.9 V. The 20 % SiO$_2$ CNFs consistently achieved superior CDI performance. Therefore, we selected them for further improvement through micropore etching to create hierarchically porous CNFs.

3.3. Characterization of hierarchically porous nanofibers

The microporosity treatment with KOH was performed with a KOH to CNF mass loading of 2:1, and treatment temperature was varied (700 °C, 750 °C, 800 °C, and 850 °C) to determine the optimal conditions to improve electrochemical and CDI performance. Increasing mass loading past this 2:1 ratio caused significant physical degradation of the fibers at the higher treatment temperatures (>750 °C). Raman and XPS spectra of various KOH-treated fibers and the micropore size distribution obtained by DFT calculation (QSDFT adsorption) are shown in Fig. 5. In all KOH-treated samples, the addition of SiO$_2$ improved both SSA and pore volume when compared to KOH-treated 0 % SiO$_2$ fibers. The hierarchically porous fibers maintained a typical Type IV(A) isotherm, as shown in Fig. S2, with increased total gas adsorption for the KOH-treated samples. The SSA and pore volume of each sample is shown in Table 2. The 0 % SiO$_2$ fibers that were KOH treated at 800 °C exhibited the lowest SSA at 1160 m^2 g^{-1}, with a pore volume of only 0.20 cc g^{-1}, compared to 1645 m^2 g^{-1} and 0.91 cc g^{-1} for the SiO$_2$ mesoporous CNFs that were KOH treated at the same temperature. The 750 °C KOH treatment temperature provided the highest SSA of 1981 m^2 g^{-1}. Other KOH treatment temperatures provided similar SSA, with 850 °C being the lowest at 1423 m^2 g^{-1}. Pore volume increased significantly in SiO$_2$ pore formed fibers at treatment temperatures of 750 °C and higher, exceeding the pore volumes obtained in the previously shown mesoporous fibers by over two times. This increase is attributed to the increase in microporosity along with the widening of the larger pores during the second thermal treatment. As shown in Fig. 5A, each KOH-treated sample exhibited significantly increased micropore volume compared to the mesoporous non-treated samples and showed similar pore size distribution in the 1.0–1.6 nm pore size range. At 800 °C, all KOH-treated fibers showed a distinct increase in micropore volume at 0.6 nm. The other KOH treatment temperatures yielded a peak shifted to ~0.8 nm. At 750 °C, the KOH treatment increased the pore volume between pore sizes of 0.8 and 2.0 nm. These differences in pore formation account for the higher surface area obtained in the 750 °C and 800 °C cases. In the 850 °C case, lower micropore volume was observed

at both 0.8 nm and 1.2 nm pore diameter, resulting in lower SSA compared to the other treatment temperatures.

Raman spectroscopy was performed to determine the effect of the KOH treatment on the structural properties of the carbon fibers, as shown in Fig. 5B. The KOH-treated fibers showed a distinct D-band at 1350 cm^{-1}, associated with defect sites, and a G-band at 1590 cm^{-1}, associated with ordered graphitic phases [42]. The non-treated fibers showed less distinction between the D and G bands, implying a more amorphous structure. The I$_D$/I$_G$ ratio, considered a measure of disorder in the graphitic lattice, was lower in the KOH-treated fibers (I$_D$/I$_G$ = 0.83) than in the non-treated CNFs (I$_D$/I$_G$ = 1.01), indicating that the thermal KOH treatment increased the degree of order in the fibers [43]. This increase in graphitization has been shown to increase electrical conductivity [44]. There was no significant difference in the I$_D$/I$_G$ ratio between the different KOH treatment temperatures.

XPS analysis was performed to determine the effects of varying KOH treatment temperature on fiber composition, shown in Fig. 5C and Table 3, with the O1s peak analysis shown in Fig. 5D. Oxygen and nitrogen content were observed to decrease with increasing treatment temperature. Fibers subjected to KOH treatment at 700 °C maintained a high oxygen content of 17.27 %, while the other treatment temperatures caused a reduction in oxygen content to 8.0–9.5 %. The oxygen content of the 700 °C treated fibers was similar to that of the non-KOH treated fibers (17.44 %), indicating that the 700 °C treatment did not remove surface oxygen groups, leading to higher C—O bonding, as shown in Fig. 5D [45]. Carbon oxidation is a primary failure mechanism for CDI electrodes, and increased oxygen content on carbon has been shown to reduce CDI performance [46]. Increased carbon oxidation can also increase the rate at which further carbon oxidation occurs, further accelerating electrode degradation during CDI operation [47]. The other KOH treatment temperatures were sufficiently high to remove surface oxygen groups and increase the total carbon percentage in the fibers, which has been shown to increase conductivity [45,48]. These results are in good agreement with the observation of lower high frequency resistance of the CNFs that were treated at higher temperature, as shown in Fig. 6A. The N1s, O1s, and C1s spectra for each treatment temperature are shown in Figs. S4, S5, and S6.

3.4. Electrochemical performance of hierarchically porous fibers

The electrochemical performance of the CNFs prepared at various KOH treatment temperatures was evaluated in 1 M NaCl using CV, GCD, and EIS, as shown in Fig. 6. We compared KOH-treated samples with and without SiO$_2$ pore former to evaluate the efficacy of the hierarchical porosity treatment. CNFs that were KOH treated at temperatures above 700 °C exhibited typical rectangular capacitive profiles at 2 mv s^{-1} in CV, as shown in Fig. 6B, while CNF that was KOH treated at 700 °C showed a sloped shape, indicating higher resistance and slower ion diffusion [49,50]. The double layer regions of the CNFs treated at 750 °C, 800 °C, and 850 °C were similar, with one difference being the slight rounding upon sweep reversal in the 20 % SiO$_2$, 750 °C and the 0 % SiO$_2$, 800 °C KOH treated samples. This slower response is attributed to the higher resistance in both cases, limiting the ability of those electrodes to respond to potential shifts [49]. The double layer capacitances of the 20 % SiO$_2$, 750 °C and the 0 % SiO$_2$, 800 °C were similar

Table 2
BET surface area and pore volume of KOH treated fibers measured using N$_2$ adsorption.

Silica content	KOH treatment temperature	SSA (m^{2}g^{-1})	Pore volume (cc g^{-1})
0 %	800 °C	1160	0.20
20 %	700 °C	1575	0.50
20 %	750 °C	1981	1.09
20 %	800 °C	1647	0.91
20 %	850 °C	1423	0.95

Table 3
Carbon, nitrogen, and oxygen contents (atomic percentage) of fibers after KOH treatment at various temperatures obtained via XPS.

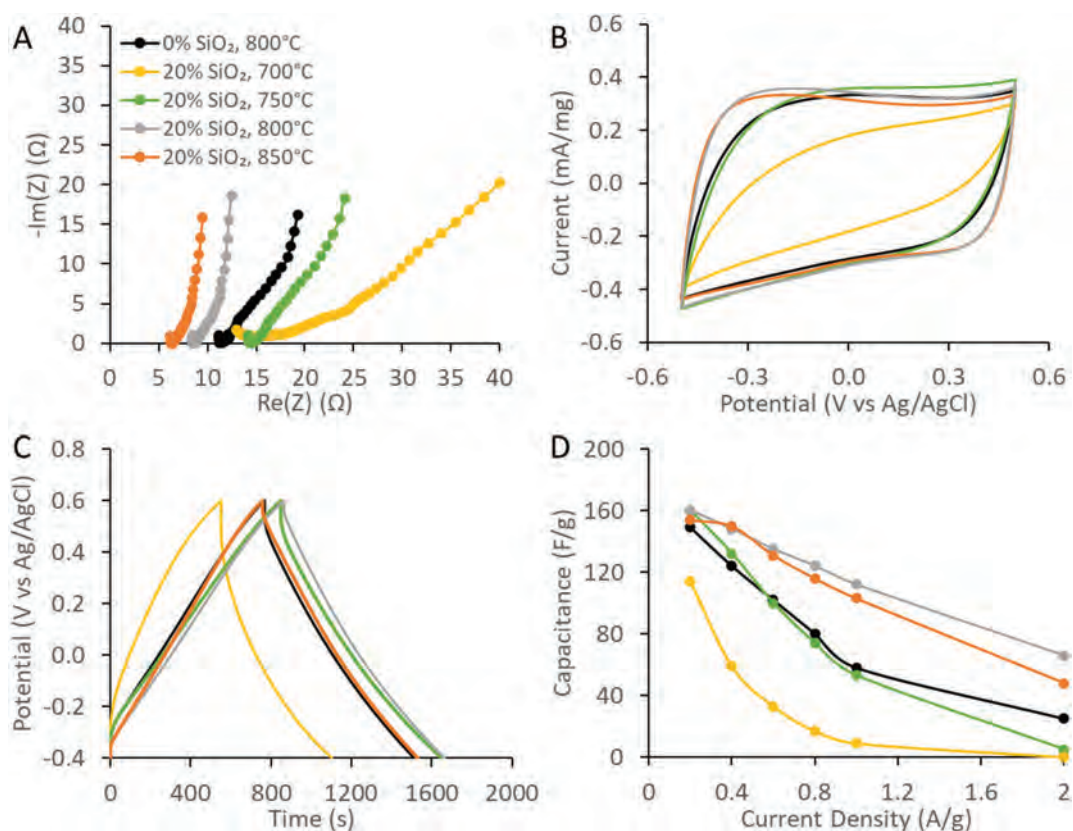| KOH treatment temp	C %	N %	O %
None	77.27	2.41	17.44
700 °C	79.63	3.1	17.27
750 °C	88.02	2.32	9.56
800 °C	90.49	1.47	8.04
850 °C	89.58	0.68	9.75

Fig. 6. Electrochemical measurements in 1 M NaCl of CNFs prepared using various KOH treatment temperatures. A) EIS spectra. B) Cyclic voltammetry (2 mv s^{-1}). C) GCD curves at 0.2 A g^{-1}. D) Capacitance versus current density obtained by GCD.

despite large differences in SSA, suggesting that part of the SSA measured in N$_2$ adsorption was not accessible for ion adsorption. The resistance of each sample was evaluated using EIS, as shown in Fig. 6A. The high-frequency resistance, associated with the ohmic resistance of the electrode, decreased with increasing treatment temperature from a high of 15 Ω in the 700 °C and 750 °C KOH treated sample to a low of 6 Ω in the 850 °C KOH treated sample. CNFs treated at higher temperatures exhibited more capacitive behavior at low frequencies, evidenced by steeper slopes, indicating that a minimum temperature of 800 °C is necessary to optimize the conductivity and capacitive response of the electrodes. The addition of mesopores formed from SiO$_2$ dissolution resulted in a decrease in high-frequency resistance from 11.6 Ω to 8.6 Ω. Adding porosity through SiO$_2$ pore formation improved capacitive behavior by facilitating ion transport, while also increasing fiber flexibility, resulting in more uniform compression and reduced contact resistance.

The capacitance of each sample was evaluated using GCD, as shown in Fig. 6C and D. Aside from the 700 °C KOH-treated sample, each sample showed a similar capacitance at 0.2 A g^{-1} of ~160 F g^{-1}. The high microporosity produced by the KOH treatment resulted in a capacitance that was nearly 3× higher than that of the non-KOH treated, 20 % SiO$_2$ CNF samples (Fig. 4C). The capacitance of the 0 % SiO$_2$ CNFs at 0.2 A g^{-1} was similar to that of the other KOH-treated samples despite the lower SSA, presumably due to inaccessible SSA in the SiO$_2$ pore formed samples that inflated SSA but did not contribute to capacitance. The iR drop of these electrodes at each current density is shown in Table S4, which reveals reduced iR drop at higher KOH treatment temperatures. The 20 % SiO$_2$ fibers treated at 800 °C and 850 °C exhibited iR drops of 40 mV at 0.2 A g^{-1} and 400 mV at 2 A g^{-1}, while the other electrodes exhibited iR drops of 70–80 mV at 0.2 A g^{-1} and 700–870 mV at 2 A g^{-1}. CNFs KOH treated at 700 °C performed marginally better in GCD than the non-KOH treated, 20 % SiO$_2$ samples

at the higher rates, despite having >6× the SSA. The increase in microporosity and SSA was ineffective at increasing capacitance at higher rates because a KOH treatment temperature of 700 °C was insufficient to increase the conductivity of the carbon fiber. This lower conductivity led to poor utilization of the high SSA, possibly due to electrical isolation and slow transport of ions. The high oxygen content observed in XPS reflected the limited conductivity of the fibers [50].

Higher KOH treatment temperatures improved the rate performance of the CNFs by increasing capacitance at higher current densities, measured by GCD shown in Fig. 6D. The 20 % SiO$_2$ samples that were treated at 800 °C and 850 °C achieved the highest capacitance at high current densities due to their higher conductivity and lower iR drops combined with high porosity. The 20 % SiO$_2$, 750 °C KOH-treated sample and the 0 % SiO$_2$, 800 °C KOH-treated sample showed similar capacitances at current densities from 0.2 to 1.0 A g^{-1}. However, their capacitances diverged at higher current density due to the lower electrical conductivity of the 20 % SiO$_2$, 750 °C KOH treated sample, which prevented full ion saturation in the micropores at high rates [40]. The 0 % SiO$_2$, 800 °C KOH treated sample had lower porosity, and thus slower ion transport, compared to the 20 % SiO$_2$, 800 °C sample, which led to lower capacitance at higher rates. The higher KOH treatment temperature mitigated this shortcoming by inducing higher conductivity than the 750 °C KOH treatment, resulting in similar capacitance for both samples. A combination of higher KOH treatment temperature and mesopore formation was the most effective strategy in optimizing electrochemical performance. Use of higher KOH treatment temperatures resulted in lower high frequency resistance, while addition of mesoporosity resulted in enhanced ion transport, enabling faster ion adsorption and greater high-rate capacitance.

3.5. CDI performance of hierarchically porous fibers

Capacitive deionization performance of hierarchically porous fiber electrodes was tested using symmetrical electrodes in single-pass, constant voltage experiments using 500 ppm NaCl at 1.2 V at a flow rate of 15 mL min^{-1}, with results shown in Fig. 7. The CDI performance of each sample is shown in Table 4. Cycling behavior and the resulting SAC retention of 20 % SiO$_2$, 850 °C KOH-treated fibers is shown in Fig. 7A. Desorption at 0 V was performed for 30 min and adsorption at 1.2 V was performed for 5 min. The desorption step was held longer to allow sufficient time for full desorption of adsorbed salt. It was observed that shorter desorption steps resulted in diminished SAC, due to incomplete desorption limiting the capacity of the next cycle. Adsorption capacities versus time for the highest performing samples from each KOH treatment case are shown in Fig. 7B, while average values are summarized in Table 4. The 20 % SiO$_2$, 800 °C KOH treated fibers achieved the highest SAC at 13.4 ± 1.5 mg g^{-1}, while SACs of samples prepared under the other treatment conditions were lower. Higher KOH treatment temperatures tended to yield higher SAC due to increased conductivity and high-rate capacitance. The 0 % SiO$_2$, 800 °C KOH-treated sample reached a peak SAC of 11.1 mg g^{-1}. While the addition of SiO$_2$ improved total SAC, KOH treatment temperature was the most significant factor in achieving high SAC due to its greater impact on the electrical conductivity of the CNFs. This effect was apparent when comparing the 20 % SiO$_2$, 750 °C KOH-treated CNFs to the 0 % SiO$_2$, 800 °C KOH-treated

Table 4
SAC (mg g^{-1}) and SAR (mg g^{-1} min^{-1}) of hierarchically porous fibers with varying KOH treatment temperatures, compared to a 0 % SiO$_2$ pore former control.

Silica content (wt %)	Treatment temperature	SAC (mg g^{-1}) (n = 3)	Average SAC (30 cycles)	SAR (mg g^{-1} min^{-1}) (n = 3)
0 %	800 °C	9.9 ± 1.7	10.5	2.9 ± 0.2
20 %	700 °C	6.1 ± 0.5	N/A	3.2 ± 1.3
20 %	750 °C	8.3 ± 0.9	6.3	3.7 ± 0.6
20 %	800 °C	13.4 ± 1.5	12.2	4.1 ± 0.7
20 %	850 °C	12.8 ± 1.5	12.6	4.9 ± 0.7

CNFs. The 20 % SiO$_2$, 750 °C CNFs had higher SSA and pore volume, but lower conductivity and lower capacitance at high current density, resulting in lower SAC. The charge efficiency of these electrodes is shown in Table S2, where the 20 % SiO$_2$, 850 °C KOH-treated CNFs obtained the highest charge efficiency of 0.70 at 1.2 V. The durability of the nanofiber electrodes was evaluated by comparing the SAC of each sample during the first cycle of operation versus the last (30th) cycle of operation. The 20 % SiO$_2$, 850 °C KOH-treated fibers obtained the highest durability at 91.5 % SAC retention. Next was the 0 % SiO$_2$, 800 °C KOH-treated fibers at 88.2 % SAC retention, then the 20 % SiO$_2$, 750 °C KOH-treated fibers at 77.2 % SAC retention, and lastly the 20 % SiO$_2$, 800 °C KOH-treated fibers at 73.4 % SAC retention. The durability of the 20 % SiO$_2$, 700 °C KOH-treated fibers was not evaluated due to
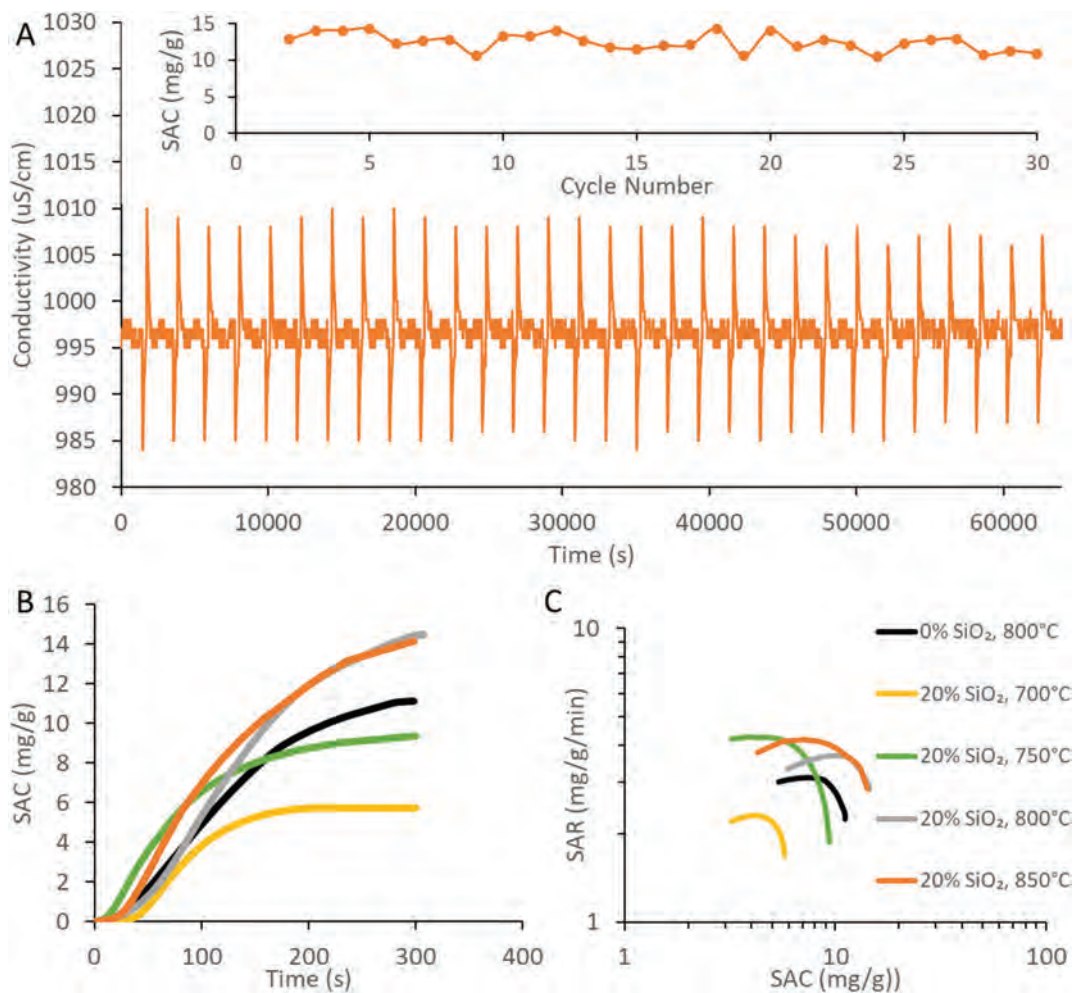

Fig. 7. Constant voltage desalination of KOH treated CNFs performed in 500 ppm NaCl at 1.2 V, 15 mL min^{-1} flow rate. A) Conductivity vs time cycling data of 20 % SiO$_2$ 850 °C KOH treated fibers. Inset shows SAC vs cycle number. B) SAC versus time and C) Ragone plot of KOH-treated CNF obtained by constant voltage desalination.

significant capacity fade that resulted in negligible capacity after only 10 cycles. The average SAC over 30 cycles was measured to evaluate average desalination output of the electrodes over a certain time, accounting for cycle-to-cycle SAC variation. The 20 % SiO_2, 850 °C KOH-treated fibers maintained an average of 12.6 mg g^{-1} over 30 cycles (88 % of peak SAC). The 20 % SiO_2, 800 °C KOH treated fibers performed similarly, averaging 12.2 mg g^{-1} over 30 cycles (85 % of peak SAC). The 0 % SiO_2, 800 °C KOH treated fibers maintained an average of 10.5 mg g^{-1} (95 % of peak SAC). Side reactions involving carbon corrosion during voltage cycling are known to cause loss of SAC, and thereby limit the effective voltage range [47,51]. Variations in pH at the electrodes have been shown to facilitate these side reactions, causing increased degradation [52,53]. The CNFs with lower KOH treatment temperatures had the largest decrease in average SAC versus peak, only maintaining 68 % of peak SAC in the 750 °C KOH treatment case. This significant capacity fade was presumably a result of the high oxygen content in these samples, leading to more rapid oxidation and performance decay. The higher-temperature KOH treatment stabilized cycling performance, improving durability over 30 cycles at 1.2 V.

The Ragone plot in Fig. 7C shows SAR versus SAC of the CNF samples, with the average SAR of 3 experiments shown in Table 4. The 20 % SiO_2, 850 °C KOH treated fibers reached the highest average SAR at 4.9 ± 0.7 mg g^{-1} min^{-1}, while the samples prepared under other treatment conditions exhibited lower SAR. The increased mesoporosity of the CNFs prepared using SiO_2 pore former allowed for fast ion transport and increased SAR relative to the 0 % SiO_2, 800 °C KOH treated sample, which exhibited the lowest SAR of 2.9 ± 0.2 mg g^{-1} min^{-1}. The 800 °C and 850 °C KOH treated, SiO_2 fiber electrodes outperformed the 0 % SiO_2 fibers in SAC and SAR, further showing how hierarchical porosity improved performance and allowed for improved ion transport and increased SSA by building micropores on existing mesopores. The low

SAC of the samples that were KOH treated at 750 °C and 700 °C highlights the need for higher temperature KOH treatments to improve the electrical properties of the fibers. The high microporosity generated by these lower temperature treatments did not increase performance enough to offset the high resistance and low capacitance at high current densities. The SAC versus capacitance of fibers developed in this work is compared to other carbon-based CDI electrodes in Fig. S7. These fibers exhibit superior, or comparable, SACs to most other electrospun CF-based CDI electrodes. The work presented here obtains comparable SAC to other high-performance electrodes, including those that use composites of activated carbon, graphene, or carbon nanotubes. The capacitance of these hierarchically porous fibers is not as high as one might expect given the large surface areas obtained. Improvements can be made to increase the surface area utilization of these electrodes and thereby maximize their capacitance.

3.6. Modeling of hierarchically porous fiber systems

To further evaluate the effect of mixed mesoporosity and microporosity on ion adsorption kinetics, pore scale modeling was performed, shown in Fig. 8. With the total porosity fixed at 0.5, the ratio of mesopores to micropores was varied along with the ion adsorption rate constants to determine how different pore structures affect the total available adsorption sites at steady state. At the lower adsorption rate constants, the total number of adsorption sites was found to increase with increasing microporosity. This is expected because at low adsorption rates, diffusion is fast compared to adsorption. As a result, ions have sufficient time to diffuse into the micropores deep in the core (which are more difficult to reach) and contact more carbon surface, resulting in more adsorption. As the rate constant increases, adsorption becomes fast compared to diffusion and the latter becomes the limiting factor of the
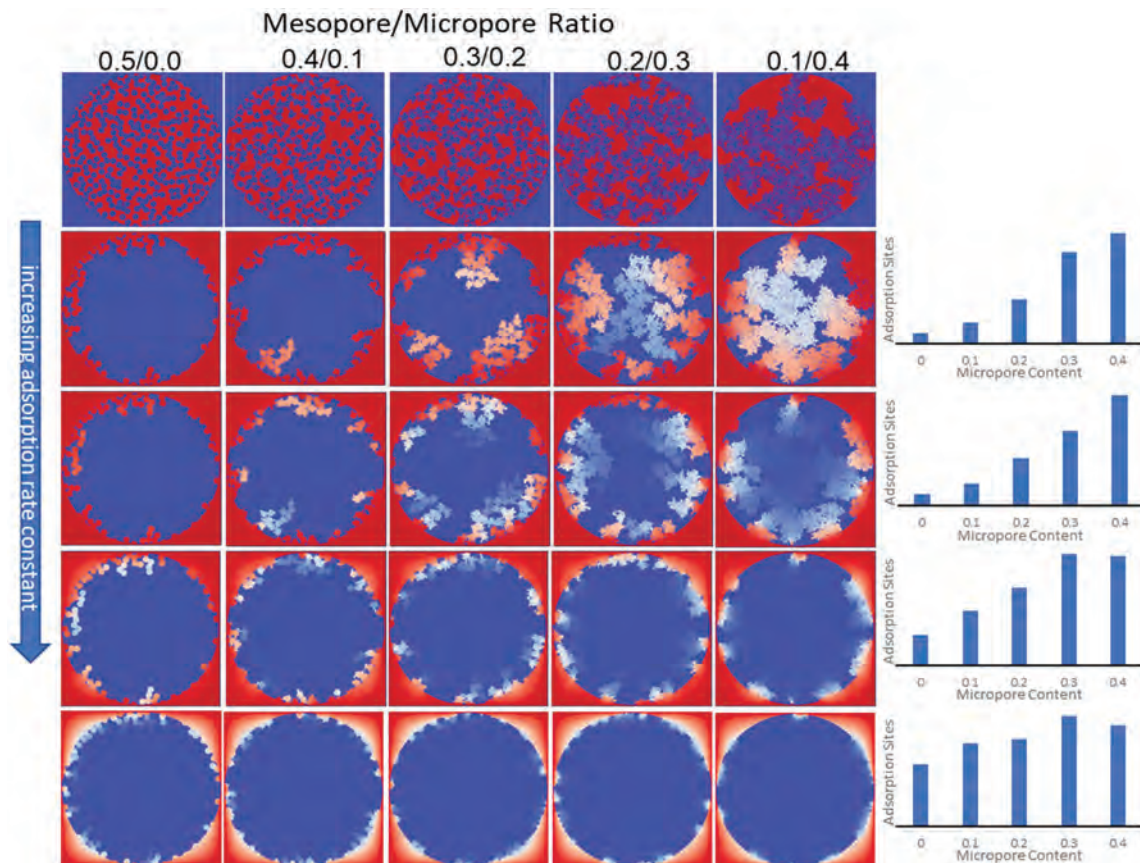

Fig. 8. Pore scale modeling results of fibers with varying adsorption rate constant and mesopore/micropore ratio, where total porosity is fixed. Total adsorption sites versus micropore content for each adsorption rate constant is shown on the right. Adsorption sites are normalized at each adsorption rate.

reaction-adsorption process. Ions are quickly adsorbed at the pore walls near the fiber surface and are not able to diffuse into pores deep in the fiber core. Consequently, mesopores near the fiber surface contribute to most of the adsorption as they facilitate ion transport, while the majority of the inner pores are ineffective. In this case, the maximum adsorption is achieved at a balanced mesoporosity and microporosity. This modeling result is reflected in the experimental data, wherein hierarchically porous CNFs with mixed meso- and microporosity outperformed predominantly-microporous CNFs. This model focused on the meso/micropore ratio in the fibers, but other factors such as pore distribution, connectivity, and tortuosity play critical roles in determining ion transport. Future models should include consideration of these more complicated metrics to further understand how porosity affects ion adsorption.

4. Conclusion

In conclusion, we have fabricated hierarchically porous CNFs using electrospun PAN precursor with inclusion of SiO_2 pore former for mesopore generation, followed by carbonization, SiO_2 dissolution, and high-temperature KOH etching for micropore formation. The mesoporosity of the CNFs was controlled by varying the amount of SiO_2 pore former, obtaining a controlled pore size distribution. The addition of mesoporosity improved electrochemical and CDI performance compared to non-porous CNFs. An optimal loading of 20 % SiO_2 pore former provided maximum CDI performance. High-temperature KOH treatment was used to further improve CDI performance by adding microporosity to the mesoporous fibers, yielding a hierarchical pore structure. The KOH treatment temperature was varied between 700 °C and 850 °C to examine its impact on CNF morphology and electrochemical/CDI performance. Treatment temperatures of at least 800 °C were the most effective at increasing electrochemical and CDI performance. Hierarchically porous CNFs prepared using SiO_2 pore former to impart mesoporosity and high-temperature KOH treatment to impart microporosity outperformed purely microporous fibers (prepared without SiO_2 pore former) in high-rate capacitance, SAC, and SAR. A mixture of meso- and microporosity was found to provide optimal CNF performance. This observation was confirmed using pore-scale modeling to determine optimal mesopore/micropore ratios at various adsorption rates, showing that as adsorption rate increases there is a greater need for balanced meso- and microporosity. The best performing hierarchically-porous fibers achieved peak SAC of >14 mg g^{-1}, peak SAR of ~3.7–4 mg g^{-1} min^{-1}, and average SAC >85 % of peak SAC over 30 cycles. This work demonstrates the viability of tailoring hierarchical porosity to improve CDI performance with carbon-based electrodes.

CRediT authorship contribution statement

John B. Waugh: Conceptualization, Investigation, Methodology, Writing – original draft, Writing – review & editing. **Siddharth Komini Babu:** Conceptualization, Funding acquisition, Investigation, Methodology, Supervision, Writing – review & editing. **Qinjun Kang:** Investigation, Methodology, Supervision, Writing – original draft, Writing – review & editing. **Nicole K. Moehring:** Investigation. **Angelica Benavidez:** Investigation. **Xiaojing Wang:** Investigation. **Piran R. Kidambi:** Supervision. **Peter N. Pintauro:** Supervision, Writing – review & editing. **Jacob S. Spendelow:** Conceptualization, Funding acquisition, Methodology, Supervision, Writing – review & editing.

Declaration of competing interest

The authors declare that they have no known competing financial interests or personal relationships that could have appeared to influence the work reported in this paper.

Data availability

Data will be made available on request.

Appendix A. Supplementary data

Supplementary data to this article can be found online at https://doi.org/10.1016/j.desal.2024.117610.

References

[1] UN, Global Issues-Water, United Nations, 2020. https://www.un.org/en/global-issues/water.
[2] E. Jones, M. Qadir, M.T.H. van Vliet, V. Smakhtin, S. Kang, The state of desalination and brine production: a global outlook, Sci. Total Environ. 657 (2019) 1343–1356, https://doi.org/10.1016/j.scitotenv.2018.12.076.
[3] J. Eke, A. Yusuf, A. Giwa, A. Sodiq, The global status of desalination: an assessment of current desalination technologies, plants and capacity, Desalination 495 (2020) 114633, https://doi.org/10.1016/j.desal.2020.114633.
[4] P. Sharan, T.J. Yoon, S.M. Jaffe, T. Ju, R.P. Currier, A.T. Findikoglu, Can capacitive deionization outperform reverse osmosis for brackish water desalination? Clean Eng Technol. 3 (2021) 100102 https://doi.org/10.1016/j.clet.2021.100102.
[5] S.Y. Pan, A.Z. Haddad, A. Kumar, S.W. Wang, Brackish water desalination using reverse osmosis and capacitive deionization at the water-energy nexus, Water Res. 183 (2020) 116064, https://doi.org/10.1016/j.watres.2020.116064.
[6] E.M. Remillard, A.N. Shocron, J. Rahill, M.E. Suss, C.D. Vecitis, A direct comparison of flow-by and flow-through capacitive deionization, Desalination 444 (2018) 169–177, https://doi.org/10.1016/j.desal.2018.01.018.
[7] K. Wang, Z. Zhang, Q. Sun, P. Wang, Y. Li, Durian shell-derived N, O, P-doped activated porous carbon materials and their electrochemical performance in supercapacitor, J. Mater. Sci. 55 (2020) 10142–10154, https://doi.org/10.1007/s10853-020-04740-1.
[8] H. Wang, H. Niu, H. Wang, W. Wang, X. Jin, H. Wang, H. Zhou, T. Lin, Micro-meso porous structured carbon nanofibers with ultra-high surface area and large supercapacitor electrode capacitance, J. Power Sources 482 (2021) 228986, https://doi.org/10.1016/j.jpowsour.2020.228986.
[9] Y. Jiang, J. Li, Z. Jiang, M. Shi, R. Sheng, Z. Liu, S. Zhang, Y. Cao, T. Wei, Z. Fan, Large-surface-area activated carbon with high density by electrostatic densification for supercapacitor electrodes, Carbon N Y. 175 (2021) 281–288, https://doi.org/10.1016/j.carbon.2021.01.016.
[10] Y. Chen, M. Yue, Z.-H. Huang, F. Kang, Electrospun carbon nanofiber networks from phenolic resin for capacitive deionization, Chem. Eng. J. 252 (2014) 30–37, https://doi.org/10.1016/j.cej.2014.04.099.
[11] G. Wang, B. Qian, Q. Dong, J. Yang, Z. Zhao, J. Qiu, Highly mesoporous activated carbon electrode for capacitive deionization, Sep. Purif. Technol. 103 (2013) 216–221, https://doi.org/10.1016/j.seppur.2012.10.041.
[12] G. Luo, Y. Wang, L. Gao, D. Zhang, T. Lin, Graphene bonded carbon nanofiber aerogels with high capacitive deionization capability, Electrochim. Acta 260 (2018) 656–663, https://doi.org/10.1016/j.electacta.2017.12.012.
[13] X. Liu, H. Liu, M. Mi, W. Kong, Y. Ge, J. Hu, Nitrogen-doped hierarchical porous carbon aerogel for high-performance capacitive deionization, Sep. Purif. Technol. 224 (2019) 44–50, https://doi.org/10.1016/j.seppur.2019.05.010.
[14] W. Dianbudiyanto, S.H. Liu, Outstanding performance of capacitive deionization by a hierarchically porous 3D architectural graphene, Desalination 468 (2019) 114069, https://doi.org/10.1016/J.DESAL.2019.07.009.
[15] G. Zhu, W. Wang, X. Li, J. Zhu, H. Wang, L. Zhang, Design and fabrication of a graphene/carbon nanotubes/activated carbon hybrid and its application for capacitive deionization, RSC Adv. 6 (2016) 5817–5823, https://doi.org/10.1039/C5RA23547B.
[16] G. Wang, Q. Dong, Z. Ling, C. Pan, C. Yu, J. Qiu, Hierarchical activated carbon nanofiber webs with tuned structure fabricated by electrospinning for capacitive deionization, J. Mater. Chem. 22 (2012) 21819, https://doi.org/10.1039/c2jm34890j.
[17] G. Wang, C. Pan, L. Wang, Q. Dong, C. Yu, Z. Zhao, J. Qiu, Activated carbon nanofiber webs made by electrospinning for capacitive deionization, Electrochim. Acta 69 (2012) 65–70, https://doi.org/10.1016/j.electacta.2012.02.066.
[18] E. Frank, F. Hermanutz, M.R. Buchmeiser, Carbon fibers: precursors, manufacturing, and properties, Macromol Mater Eng. 297 (2012) 493–501, https://doi.org/10.1002/mame.201100406.
[19] A.G. El-Deen, N.A.M. Barakat, K.A. Khalil, H.Y. Kim, Development of multi-channel carbon nanofibers as effective electrosorptive electrodes for a capacitive deionization process, J Mater Chem A Mater. 1 (2013) 11001, https://doi.org/10.1039/c3ta12450a.
[20] G. Wang, B. Qian, Y. Wang, Q. Dong, F. Zhan, J. Qiu, Electrospun porous hierarchical carbon nanofibers with tailored structures for supercapacitors and

capacitive deionization, New J. Chem. 40 (2016) 3786–3792, https://doi.org/10.1039/c5nj02963e.

[21] H. Zhang, Z. Xie, Y. Wang, X. Shang, P. Nie, J. Liu, Electrospun polyacrylonitrile/β-cyclodextrin based porous carbon nanofiber self-supporting electrode for capacitive deionization, RSC Adv. 7 (2017) 55224–55231, https://doi.org/10.1039/C7RA12001J.

[22] H. Pan, J. Yang, S. Wang, Z. Xiong, W. Cai, J. Liu, Facile fabrication of porous carbon nanofibers by electrospun PAN/dimethyl sulfone for capacitive deionization, J Mater Chem A Mater. 3 (2015) 13827–13834, https://doi.org/10.1039/c5ta02954f.

[23] T. Hussain, Y. Wang, Z. Xiong, J. Yang, Z. Xie, J. Liu, Fabrication of electrospun trace NiO-doped hierarchical porous carbon nanofiber electrode for capacitive deionization, J. Colloid Interface Sci. 532 (2018) 343–351, https://doi.org/10.1016/j.jcis.2018.07.129.

[24] J. Liu, S. Wang, J. Yang, J. Liao, M. Lu, H. Pan, L. An, ZnCl2 activated electrospun carbon nanofiber for capacitive desalination, Desalination 344 (2014) 446–453, https://doi.org/10.1016/j.desal.2014.04.015.

[25] Y. Zhao, G. Luo, L. Zhang, L. Gao, D. Zhang, Z. Fan, Nitrogen-doped porous carbon tubes composites derived from metal-organic framework for highly efficient capacitive deionization, Electrochim. Acta 331 (2020) 135420, https://doi.org/10.1016/j.electacta.2019.135420.

[26] O. Noonan, Y. Liu, X. Huang, C. Yu, Layered graphene/mesoporous carbon heterostructures with improved mesopore accessibility for high performance capacitive deionization, J Mater Chem A Mater. 6 (2018) 14272–14280, https://doi.org/10.1039/C8TA03114B.

[27] S.K. Mohamed, S.A. Elsalam, A. Shahat, H.M.A. Hassan, R.M. Kamel, Efficient sucrose-derived mesoporous carbon sphere electrodes with enhanced hydrophilicity for water capacitive deionization at low cell voltages, New J. Chem. 45 (2021) 1904–1914, https://doi.org/10.1039/D0NJ05412G.

[28] S. Porada, L. Weinstein, R. Dash, A. van der Wal, M. Bryjak, Y. Gogotsi, P. M. Biesheuvel, Water desalination using capacitive deionization with microporous carbon electrodes, ACS Appl. Mater. Interfaces 4 (2012) 1194–1199, https://doi.org/10.1021/am201683j.

[29] P.M. Biesheuvel, S. Porada, M. Levi, M.Z. Bazant, Attractive forces in microporous carbon electrodes for capacitive deionization, J. Solid State Electrochem. 18 (2014) 1365–1376, https://doi.org/10.1007/s10008-014-2383-5.

[30] M. Kim, X. Xu, R. Xin, J. Earnshaw, A. Ashok, J. Kim, T. Park, A.K. Nanjundan, W. A. El-Said, J.W. Yi, J. Na, Y. Yamauchi, KOH-activated hollow ZIF-8 derived porous carbon: nanoarchitectured control for upgraded capacitive deionization and supercapacitor, ACS Appl. Mater. Interfaces 13 (2021) 52034–52043, https://doi.org/10.1021/acsami.1c09107.

[31] S.-H. Yoon, S. Lim, Y. Song, Y. Ota, W. Qiao, A. Tanaka, I. Mochida, KOH activation of carbon nanofibers, Carbon N Y. 42 (2004) 1723–1729, https://doi.org/10.1016/j.carbon.2004.03.006.

[32] H. Zhang, C. Wang, W. Zhang, M. Zhang, J. Qi, J. Qian, X. Sun, B. Yuliarto, J. Na, T. Park, H.G.A. Gomaa, Y.V. Kaneti, J.W. Yi, Y. Yamauchi, J. Li, Nitrogen, phosphorus co-doped eave-like hierarchical porous carbon for efficient capacitive deionization, J Mater Chem A Mater. 9 (2021) 12807–12817, https://doi.org/10.1039/D0TA10797B.

[33] L. Chen, H.-B. Luan, Y.-L. He, W.-Q. Tao, Pore-scale flow and mass transport in gas diffusion layer of proton exchange membrane fuel cell with interdigitated flow fields, Int. J. Therm. Sci. 51 (2012) 132–144, https://doi.org/10.1016/j.ijthermalsci.2011.08.003.

[34] S. Arbab, A. Zeinolebadi, Quantitative analysis of the effects of comonomers and heating conditions on the stabilization reactions of polyacrylonitrile fibers as carbon fiber precursors, Polym. Degrad. Stab. 139 (2017) 107–116, https://doi.org/10.1016/j.polymdegradstab.2017.04.003.

[35] F. Sotomayor, K. Cychosz, M. Thommes, Characterization of Micro/Mesoporous Materials by Physisorption: Concepts and Case Studies, 2018.

[36] A.A. Hor, S.A. Hashmi, Optimization of hierarchical porous carbon derived from a biomass pollen-cone as high-performance electrodes for supercapacitors, Electrochim. Acta 356 (2020) 136826, https://doi.org/10.1016/j.electacta.2020.136826.

[37] M. Thommes, K. Kaneko, A.V. Neimark, J.P. Olivier, F. Rodriguez-Reinoso, J. Rouquerol, K.S.W. Sing, Physisorption of gases, with special reference to the evaluation of surface area and pore size distribution (IUPAC Technical Report),

Pure and Applied Chemistry 87 (2015) 1051–1069, https://doi.org/10.1515/pac-2014-1117.

[38] D.I. Abouelamaiem, G. He, T.P. Neville, D. Patel, S. Ji, R. Wang, I.P. Parkin, A. B. Jorge, M.-M. Titirici, P.R. Shearing, D.J.L. Brett, Correlating electrochemical impedance with hierarchical structure for porous carbon-based supercapacitors using a truncated transmission line model, Electrochim. Acta 284 (2018) 597–608, https://doi.org/10.1016/j.electacta.2018.07.190.

[39] K. Mahankali, N.K. Thangavel, Y. Ding, S.K. Putatunda, L.M.R. Arava, Interfacial behavior of water-in-salt electrolytes at porous electrodes and its effect on supercapacitor performance, Electrochim. Acta 326 (2019) 134989, https://doi.org/10.1016/j.electacta.2019.134989.

[40] I. Yang, S.-G. Kim, S.H. Kwon, M.-S. Kim, J.C. Jung, Relationships between pore size and charge transfer resistance of carbon aerogels for organic electric double-layer capacitor electrodes, Electrochim. Acta 223 (2017) 21–30, https://doi.org/10.1016/j.electacta.2016.11.177.

[41] G. Zhang, T. Guan, N. Wang, J. Wu, J. Wang, J. Qiao, K. Li, Small mesopore engineering of pitch-based porous carbons toward enhanced supercapacitor performance, Chem. Eng. J. 399 (2020) 125818, https://doi.org/10.1016/j.cej.2020.125818.

[42] Z. Xu, J. Li, X. Li, Z. Chen, C. Chen, S.A. Ali Shah, M. Wu, An instantaneous metal organic framework to prepare ultra-high pore volume porous carbon for lithium ion capacitors, Appl. Surf. Sci. 565 (2021) 150528, https://doi.org/10.1016/j.apsusc.2021.150528.

[43] J. Jiang, J. Yuan, P. Nie, Q. Zhu, C. Chen, W. He, T. Zhang, H. Dou, X. Zhang, Hierarchical N-doped hollow carbon microspheres as advanced materials for high-performance lithium-ion capacitors, J Mater Chem A Mater. 8 (2020) 3956–3966, https://doi.org/10.1039/C9TA08676E.

[44] X. Li, C. Hao, B. Tang, Y. Wang, M. Liu, Y. Wang, Y. Zhu, C. Lu, Z. Tang, Supercapacitor electrode materials with hierarchically structured pores from carbonization of MWCNTs and ZIF-8 composites, Nanoscale 9 (2017) 2178–2187, https://doi.org/10.1039/C6NR08987A.

[45] W. Chen, M. Gong, K. Li, M. Xia, Z. Chen, H. Xiao, Y. Fang, Y. Chen, H. Yang, H. Chen, Insight into KOH activation mechanism during biomass pyrolysis: chemical reactions between O-containing groups and KOH, Appl. Energy 278 (2020) 115730, https://doi.org/10.1016/j.apenergy.2020.115730.

[46] E. Avraham, M. Noked, Y. Bouhadana, A. Soffer, D. Aurbach, Limitations of charge efficiency in capacitive deionization processes III: the behavior of surface oxidized activated carbon electrodes, Electrochim. Acta 56 (2010) 441–447, https://doi.org/10.1016/j.electacta.2010.08.056.

[47] I. Cohen, E. Avraham, Y. Bouhadana, A. Soffer, D. Aurbach, Long term stability of capacitive de-ionization processes for water desalination: the challenge of positive electrodes corrosion, Electrochim. Acta 106 (2013) 91–100, https://doi.org/10.1016/j.electacta.2013.05.029.

[48] C.-K. Liu, Y. Feng, H.-J. He, J. Zhang, R.-J. Sun, M.-Y. Chen, Effect of carbonization temperature on properties of aligned electrospun polyacrylonitrile carbon nanofibers, Mater. Des. 85 (2015) 483–486, https://doi.org/10.1016/j.matdes.2015.07.021.

[49] S. Aderyani, P. Flouda, S.A. Shah, M.J. Green, J.L. Lutkenhaus, H. Ardebili, Simulation of cyclic voltammetry in structural supercapacitors with pseudocapacitance behavior, Electrochim. Acta 390 (2021) 138822, https://doi.org/10.1016/j.electacta.2021.138822.

[50] H. Zhao, B. Xing, C. Zhang, G. Huang, J. Yu, Z. Jiang, X. Qu, X. Wu, Y. Cao, C. Zhang, MnOX–modified corrugated carton–derived hierarchical porous carbon with ultrafast kinetics behaviour for high–performance symmetric supercapacitors, J. Alloys Compd. 848 (2020) 156423, https://doi.org/10.1016/j.jallcom.2020.156423.

[51] C. Zhang, D. He, J. Ma, W. Tang, T.D. Waite, Faradaic reactions in capacitive deionization (CDI) - problems and possibilities: a review, Water Res. 128 (2018) 314–330, https://doi.org/10.1016/j.watres.2017.10.024.

[52] J.E. Dykstra, K.J. Keesman, P.M. Biesheuvel, A. van der Wal, Theory of pH changes in water desalination by capacitive deionization, Water Res. 119 (2017) 178–186, https://doi.org/10.1016/j.watres.2017.04.039.

[53] J. Yu, K. Jo, T. Kim, J. Lee, J. Yoon, Temporal and spatial distribution of pH in flow-mode capacitive deionization and membrane capacitive deionization, Desalination 439 (2018) 188–195, https://doi.org/10.1016/j.desal.2018.04.011.